Deciphering the Carrier Transport Properties in Two-Dimensional Perovskites via Surface-Enhanced Raman Scattering

Yuting Zou, Zhi Yu,* Hao Ma, Chen Zhao, Bin Wang, Ruiyan Li, Xiuyun Li, Jianjun Yang, Feng Li,* and Weili Yu*

2D layered organic-inorganic perovskites have attracted substantial attention due to their high stability and promising optoelectronic properties. However, in-depth insights on the anisotropic carrier transport properties of these 2D perovskites are remaining challenging, while they are significant for further designing the high-performance device applications. Here, the carrier transport properties within 2D perovskite single crystals are investigated and a layered-carrier-transport model is developed through the non-invasive and non-destructive surface-enhanced Raman scattering techniques. The carrier transport features of 2D perovskites show clearly the thickness-, applied voltage- and anisotropy-dependent behaviors, which are demonstrated to origin from the quantum confinement effect. The findings elucidate the carrier transport mechanisms within 2D perovskites from their molecular level through Raman spectroscopy, thus providing a promising way for exploring the photo-physical properties in wide-ranged halide perovskites and designing highly efficient perovskite optoelectronic devices.

1. Introduction

Organic–inorganic hybrid perovskites have made impressive marks in the scientific community during the past decades owing to their unique optical and electrical properties, such as tunable direct bandgaps, high absorption coefficients, large photoluminescence (PL) quantum yields, high carrier mobilities, and long carrier diffusion lengths.[1–11] These extraordinary properties, combined with their compatibility of solution processing, have made this class of materials highly competitive in

the field of photovoltaic and wide-ranged optoelectronic devices. Among various perovskite materials, the lattices of 3D perovskite are easily decomposed into reactants under the conditions of ultraviolet irradiation, high temperature, or/and hydration environment, resulting in the rapid decline of device performance.[12,13] In comparison, 2D perovskites, with robust environmental stability, optoelectronic tunability, and unique quantum well structures, are becoming the rising choice of candidates for next-generation energy and optoelectronic applications.[14–17]

The 2D perovskites composed by the organic cation layer and the inorganic unit layer show unique layer-by-layer structure, which are thus endowed with distinctive properties and notable merits. The large organic ligands in the 2D perovskite lattices provide the space barriers for the surface water penetration, which can effectively inhibit the invasion of water.[18–20] In addition, the large-sized organic ligands can confine the charge carrier transport within the 2D local scope,[21] thereby affecting the photoelectric conversion efficiency. Importantly, the organic spacers also act as the dielectric regulator, which determines the electrostatic force on the electron-hole pairs, promoting the exciton radiative recombination efficiency.[22] Furthermore, the unique layered structure of 2D perovskites makes the ion movements in the films are highly dependent on their growth orientations.[23,24] Despite

Y. Zou, Z. Yu, C. Zhao, R. Li, X. Li, J. Yang, W. Yu
GPL Photonic Laboratory
State Key Laboratory of Applied Optics
Changchun Institute of Optics, Fine Mechanics and Physics
Chinese Academy of Science
Changchun 130033, China
E-mail: zhiyu@ciomp.ac.cn; weili.yu@ciomp.ac.cn
Y. Zou, Z. Yu, C. Zhao, R. Li, X. Li, J. Yang, W. Yu
University of Chinese Academy of Science
Beijing 100049, China

ⓘ The ORCID identification number(s) for the author(s) of this article can be found under https://doi.org/10.1002/smll.202103756.

H. Ma
State Key Laboratory of Physical Chemistry of Solid Surfaces
College of Chemistry and Chemical Engineering
Xiamen University
Xiamen 361005, China
B. Wang
State Key Laboratory of Applied Optics
Changchun Institute of Optics, Fine Mechanics and Physics
Chinese Academy of Science
Changchun 130033, China
F. Li
School of Physics
The University of Sydney
Sydney NSW 2006, Australia
E-mail: feng.li2@sydney.edu.au

**ADVANCED
SCIENCE NEWS**

www.advancedsciencenews.com

NANO · MICRO

small

www.small-journal.com

these promising merits of 2D perovskites, their anisotropic carrier transport properties are still lacking in-depth understandings. In this regard, unveiling the key factors and mechanisms that affect the carrier transport properties and the device performances of 2D perovskite materials is highly awarding.

Recently, the pioneering evaluations on the relationship between the material crystal orientations and the carrier transport properties are mainly based on the theoretical simulations and experimental current–voltage (I–V) behaviors that are the traditional macroscopic characterization techniques. For example, Liu's group theoretically studied the anisotropic transport properties of 2D perovskites using density function theory (DFT) calculations, which were further confirmed through measured I–V curves in the related photodetectors with different orientations.[25] Considering the accuracy and convenience, it should be highlighted that it is still highly desired to develop an optical or spectroscopic method to reveal their anisotropic transport behaviors more intuitively. Encouragingly, surface-enhanced Raman Scattering (SERS), first discovered in 1974, has been widely applied for fundamental research and the practical device applications.[26–29] It can be operated in micrometer scale and be applied in ultrasensitive analyses and detections, surface/interface analysis, and interfacial charge process studies, et al. Furthermore, such technique has also been widely utilized to analyze the structural and optoelectronic properties of the molecule-adsorbed semiconductor materials in the highly accurate and convenient way.[30,31] Particularly, SERS spectrum is extremely sensitive to the slight disturbance of the surrounding environment and the internal structure of molecules, it can thus be used for monitoring the intermolecular interaction, interfacial charge transfer, environmental changes, et al.[32] Therefore, it is expected such technique can offer an effective way to study the charge transfer and charge transport properties in 2D perovskite materials.

Herein, we study the carrier transport mechanisms and charge transfer processes of 2D perovskite materials through non-invasive and non-destructive SERS-based approach and propose a layered-carrier-transport model. We employ organic material 3,4,9,10-Perylenetetracarboxylic Dianhydride (PTCDA) as probe molecule to broaden the intrinsic photo-responsive range of 2D perovskites and investigate the carrier transport properties related to the crystal structure within 2D perovskites through photoelectric behavior and Raman spectra measurements. Systematically, the dependences of Raman intensities on 2D perovskite layer thickness, applied voltage, and crystal anisotropy are investigated. The obtained photocurrent, Raman intensity, and the dynamic PL lifetime show the clear thickness-dependent characteristics, with the optimal thickness value reaching 228 nm. Furthermore, through voltage-dependent intrinsic Raman spectra measurements, together with the reversibility of voltage polarization, we decipher the anisotropic transport properties along the different crystal orientations of the 2D perovskites. We attribute these properties to the quantum confinement effect of 2D perovskites. This study offers in-depth insights on revealing the fundamental photo-physical processes and carrier transport features within 2D perovskite materials, which could be extended to wide-range halide perovskites, holding a broad application prospect in optoelectronics.

2. Results and Discussions

2.1. Photoelectronic Characterizations on (PEA)$_2$PbBr$_4$/PTCDA Heterojunction

2D layered perovskite (PEA)$_2$PbBr$_4$ (PEA: phenethylammonium) single crystals show photoelectric response characteristics in the ultraviolet region due to their intrinsic band structure, which hinders their detection application in visible range.[33] To broaden their photo-responsive range, we fabricated the photoelectronic devices by constructing an interfacial charge transfer heterojunction with PTCDA as a sensitive layer, of which the schematic structure is illustrated in **Figure 1**a. In this heterojunction-based device, the (PEA)$_2$PbBr$_4$ single-crystal thin film was grown using solution process, and the organic PTCDA layer was deposited on the top, of which the detailed procedures are shown in the Methods section. The PTCDA molecule has a bandgap of 2.54 eV and is conducive to charge transfer process, thus it can enhance the photo-response properties of the related devices accordingly.

We further studied and compared the photoelectric response characteristics of the PTCDA-modified 2D perovskite device and the pure perovskite device without PTCDA decoration via measuring their I–V behaviors in dark and under a 532-nm laser illumination. As shown in Figure 1b, the (PEA)$_2$PbBr$_4$-PTCDA heterojunction-based device has almost no current response at 5 V in the dark; while under illumination, it shows a highly enhanced photocurrent reaching 8×10^{-7} A. In contrast, the pure (PEA)$_2$PbBr$_4$ thin single crystal device and pure PTCDA molecules device (as shown in Figure S3, Supporting Information) almost show no photo-response under the same condition. The observations can be attributed to the absorption property of the added PTCDA molecules and the effective charge transfer effect at the perovskite/PTCDA interface due to the formation of a type-II heterojunction (Figure 1c). The time-resolved photoluminescence (TRPL) measurements were further performed on the heterojunction, aiming to obtain the quantitative analyses of the charge injection and photo-induced carrier recombination at the interface. As shown in Figure 1d, when excited by a 532-nm laser, the PTCDA-modified (PEA)$_2$PbBr$_4$ thin single crystal shows a prolonged carrier lifetime (τ), with an average value (τ_{ave}) of 4.154 ns, as compared with that of the pure PTCDA molecules (2.916 ns). The result further demonstrates the formed type-II heterojunction and the existence of charge transfer from the 2D perovskite thin crystal to the PTCDA molecules, which thus enhances the probability of carrier recombination at the interface or within organic PTCDA molecules.

In order to characterize the photo-physical process between the 2D perovskite and PTCDA molecules more intuitively, SERS method is further performed to study the interfacial charge transfer process in the heterojunction. The Raman spectra of the PTCDA molecule layer deposited on the (PEA)$_2$PbBr$_4$ thin single crystal surface, along with those of the (PEA)$_2$PbBr$_4$ thin single crystal and the pure PTCDA molecules, were collected under a 532-nm laser. As shown in Figure 1e, the Raman intensity of PTCDA layer is extremely enhanced after depositing on the perovskite single crystal surface as compared with that of pure PTCDA layer and the intensity ratios of all
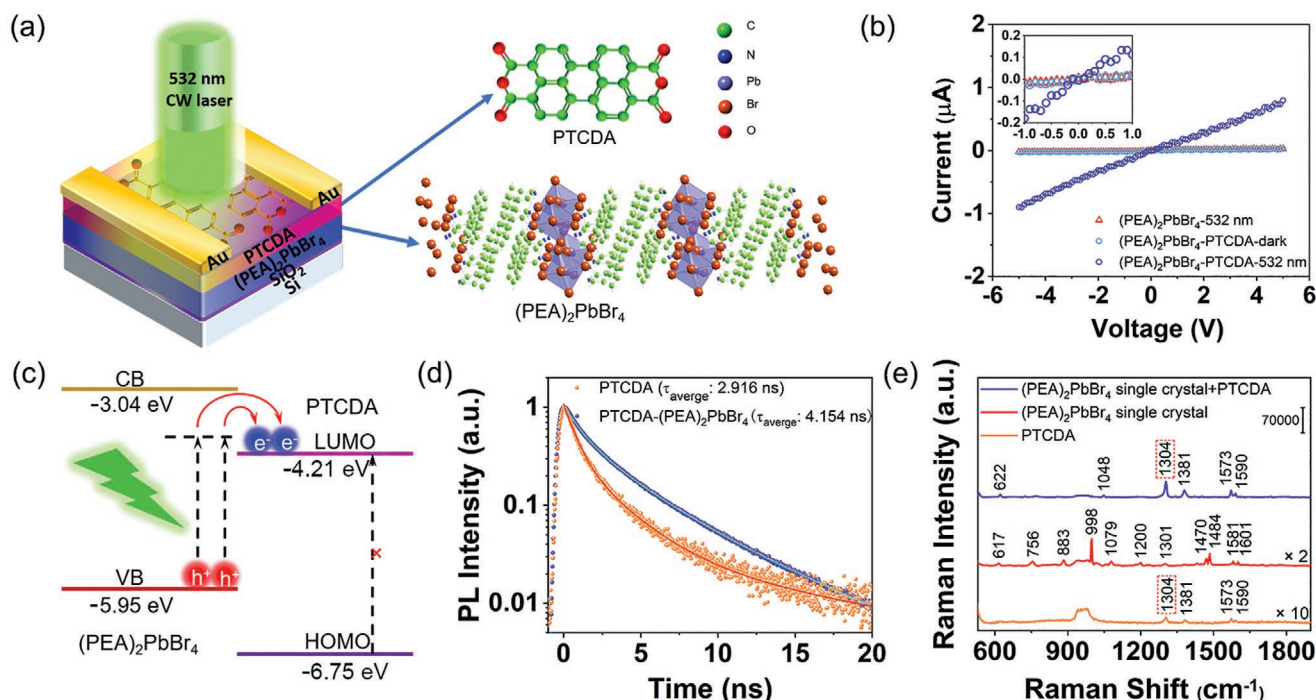
Figure 1. Enhanced photoelectric response and Raman spectra by the interfacial charge transfer. a) Schematic of $(PEA)_2PbBr_4$ thin single crystal photodetector with PTCDA layer on the top, along with crystal structures of $(PEA)_2PbBr_4$ and PTCDA molecule. b) Current–voltage (I–V) characteristics of the $(PEA)_2PbBr_4$ photodetector and $(PEA)_2PbBr_4$-PTCDA photodetector under a 532-nm illumination, as well as that of $(PEA)_2PbBr_4$-PTCDA photodetector in the dark condition. Inset: enlarged I–V curves. c) Energy level diagram of $(PEA)_2PbBr_4$-PTCDA system under a 532-nm laser excitation. d) TRPL decay curves of the PTCDA molecule and $(PEA)_2PbBr_4$-PTCDA heterojunction under a 532-nm laser at room temperature in air. e) Raman spectra of $(PEA)_2PbBr_4$-PTCDA heterojunction, $(PEA)_2PbBr_4$ thin single crystal, and PTCDA, respectively. The spectra are collected under a 532-nm laser excitation.

the bands are listed in Table S1, Supporting Information. The Raman enhancement can be attributed to the interfacial charge transfer resonance between perovskite and PTCDA, which can be proved by the increase in the prolonged lifetime of PTCDA molecules. As Table S1, Supporting Information, shows, all the characteristic bands for PTCDA molecules are enhanced by one order with some differences in the relative intensity. The change in the relative intensity may be associated with the differences in the molecular organizations after deposition on the perovskites' surface.[34] It should be noted that the PTCDA molecule exhibits obvious absorption at 532 nm (Figure S1, Supporting Information) and the resonance Raman spectra can be achieved under 532-nm laser excitation. However, in our cases, the Raman intensity of $(PEA)_2PbBr_4$-PTCDA heterojunction is much larger than that of PTCDA molecule film with the same thickness, which indicates that the resonance Raman provides extremely lower contribution to the enhanced Raman intensity. Thus, the Raman enhancement of PTCDA molecules can be attributed to the charge transfer effect between the 2D perovskites and PTCDA molecules. As is well known, in the semiconductor/molecule heterojunction system, the charge transfer process usually takes place as the electrons transit from the valence band (VB) of the semiconductors to the lowest unoccupied molecular orbital (LUMO) level of the deposited organic molecules under the laser excitation.[27,35] In our case, the VB band of the 2D perovskites is −5.95 eV (Ref. [33]), while the LUMO level of the PTCDA molecules is calculated

to be −4.21 eV from DFT (Figure S4, Supporting Information). The energy level difference is calculated to be 1.75 eV, and the heterojunction system can thus be excited by a 532-nm laser (E_g = 2.32 eV). The scheme of the photo-induced electrons transferred from the VB level of 2D perovskite to the LUMO level of PTCDA molecules, as presented in Figure 1c, explains well the enhanced photoelectric response phenomenon and the laser-induced enhanced Raman spectra.

2.2. Thickness-Dependent Photoelectric Response

Subsequently, perovskite thickness-dependent photoelectric responses of the $(PEA)_2PbBr_4$-PTCDA heterojunction photodetectors were further investigated, and the photocurrent values exhibit interesting thickness-dependent characteristics, which increase first and then decrease with the increasing thickness of the 2D perovskite (**Figure 2**a). Figure 2b summarizes the photocurrent values for the heterojunction devices with various perovskite thicknesses upon a 6-V bias obtained from Figure 2a, which clearly shows the change trend, that is, increasing first and then decreasing. In our work, the thickness of the perovskite single-crystal thin films was characterized by mechanical stripping using atomic force microscopy (AFM, Figure S5, Supporting Information).

Figure 2c shows the SERS intensities of the PTCDA molecules deposited on (001) plane of the perovskite crystals with
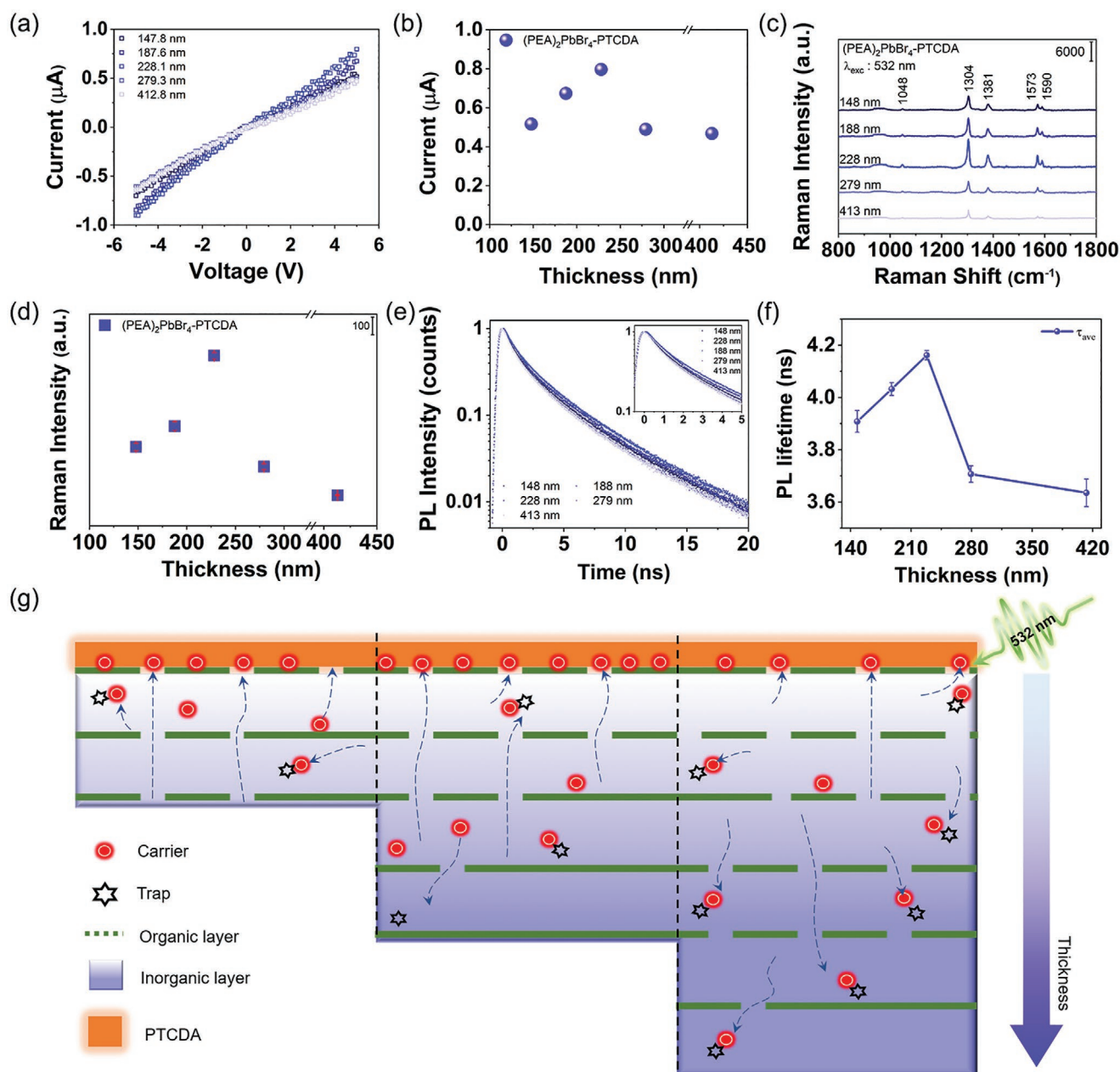
ADVANCED
SCIENCE NEWS
www.advancedsciencenews.com

NANO · MICRO
small
www.small-journal.com

Figure 2. Thickness-dependent photoelectric response and Raman spectra. a) Current–voltage (*I–V*) curves of PTCDA layer deposited on $(PEA)_2PbBr_4$ thin single crystal with varying perovskite thicknesses under a 532-nm illumination. b) Photocurrent values of the heterojunctions with varying $(PEA)_2PbBr_4$ thicknesses under a 532-nm laser excitation. c) SERS spectra of the heterojunctions with varying perovskite thicknesses under a 532-nm laser excitation. d) Raman intensity values of the heterojunctions with varying perovskite thicknesses under a 532-nm laser excitation. Raman spectra are shifted compared to each other along the *y* axis for better viewing. Error bars represent [mean ± SD (*n* = 5)]. e) Time-resolved PL decay curves of the PTCDA deposited on $(PEA)_2PbBr_4$ thin single crystals with varying thicknesses under a 532-nm laser excitation at room temperature in air. f) PL average lifetime of the PTCDA adsorbed on $(PEA)_2PbBr_4$ thin single crystals with varying thicknesses. g) Schematic diagram of layered carrier transport model for the 2D perovskite-based heterojunctions with the different perovskite thicknesses.

the varied thicknesses. The results from Figure 2c on the Raman intensities measured at 622, 1304, 1381, 1573, 1590 cm^{-1} of the PTCDA layer deposited on the various-thickness $(PEA)_2PbBr_4$ layers are summarized in Figure 2d and Figure S6, Supporting Information, which indicates the same change trend as the photocurrent case and shows a maximum Raman value at the thickness of 228 nm upon a 532-nm irradiation.

Meanwhile, the SERS mapping measurements at 1304 cm^{-1} were also carried out under illumination at a 532-nm laser. Figure S7a, Supporting Information, shows the camera view of the scanning area, where the different colors indicate the thickness variation of the 2D perovskite thin crystal. The relevant Raman mapping analysis result is shown in Figure S7b, Supporting Information, in which the different colors represent

**ADVANCED
SCIENCE NEWS**

www.advancedsciencenews.com

NANO · MICRO

small

www.small-journal.com

the different Raman intensities, consistent with the thickness distribution of the 2D perovskite. To further explore the mechanism on the thickness-dependent carrier transport properties, the TRPL spectra of the PTCDA deposited on $(PEA)_2PbBr_4$ single-crystal film with varying thicknesses were measured using a 532-nm picosecond laser in air at room temperature (see Figure 2e). The dependence of τ_{ave} of heterojunction with the $(PEA)_2PbBr_4$ thickness is plotted in Figure 2f. With the perovskite thickness increasing, the τ_{ave} exhibits similar thickness-dependent trend as the cases of photocurrent and Raman intensity, which means that the thickness of 2D perovskite crystals has the key role on their carrier transport behaviors. Generally, the thickness-related phenomenon observed in the 3D perovskite single crystal can be attributed to the variation of the surface-layer thickness with the increasing crystal thickness.[36] Due to the special layer-by-layer structure of the 2D perovskite, the carrier transport is affected by not only the defects but also the quantum well structure formed by alternately arranged organic and inorganic layers. In this regard, we propose a layered-carrier-transport model to explain the layer-dependent carrier transport properties in 2D perovskites, as shown in Figure 2g. Normally, the light-excited electrons can transit to the virtual energy level of the 2D perovskite and then transfer to the LUMO level of the molecular layer due to the matched energy alignment, and they can be captured by the electrodes. In the 2D perovskite system, cracks in the organic cation layer can form interlayer "tunnels", providing a path for bottom-up carrier transport. In a certain thickness range, with the increase of perovskite layer thicknesses, the charge carriers generated in the "shallow" perovskite transmit upward through the "defect tunnel" within the organic cation layer and then transfer to the PTCDA molecules. The charge accumulation and bottom-up carrier transport can promote the charge transfer between the 2D perovskite and the PTCDA molecules, which results in the enhancements of SERS intensity and photocurrent. When the thickness of perovskite layers continues to increase, the "deep" perovskites beyond the effective photo-induced carrier transport range not only affect the carrier extraction but also lead to more undesirable traps in the inorganic layer, which will capture the carriers generated in the "shallow" perovskite. This process inhibits the charge transfer from the 2D perovskite to the PTCDA molecules, and thus both the SERS intensity and the photocurrent are reduced. According to the above analysis, the relationship between SERS results and photoelectric values can be established based on the interfacial charge transfer process. At this point, SERS can be taken as a novel tool for monitoring the charge transfer process for the 2D perovskite/organic heterojunction, and organic material is not only a sensitive layer for enhancing the photoelectric response but also a probe molecule for monitoring the internal charge transfer process.

2.3. SERS Measurements on 2D Perovskite Bulk Single Crystal

To gain further insights into the carrier transport properties caused by the quantum confinement effect within 2D perovskites, the Raman spectroscopy measurements on the bulk 2D perovskites without PTCDA modification were performed to study the electron transport behaviors inside 2D perovskite materials with different crystal orientations under external voltage bias. The PEA cations in the organic layers of the 2D perovskite can be taken as the probe molecule for the SERS measurements. To achieve the goal, the Au electrodes (20 mm × 5 mm) were deposited on the (001) and (010) planes of $(PEA)_2PbBr_4$ bulk single crystal with a size of 8 mm × 3 mm, respectively (shown in **Figure 3**a and Figure S8a, Supporting Information, respectively), and the relevant microscope images of the devices after the deposition of Au electrodes are shown in the inset of each figure. Figure S9, Supporting Information shows the photo image of the bulk perovskite. The Raman spectra were then collected in the 2D perovskite with (001) and (010) planes under open circuit condition, short circuit condition, and load condition. The Raman spectra of PEABr powder, $PbBr_2$ powder, (001) plane and (010) plane of $(PEA)_2PbBr_4$ single crystal are shown in Figure S10, Supporting Information, and the Raman band assignment for PEABr is listed in Table S2, Supporting Information. The results indicate that the characteristic peaks of Raman spectra of (001) and (010) planes of 2D perovskite crystal are different due to the different molecule orientations exposed by different lattice planes. Furthermore, obvious Raman spectra changes occur between open circuit condition and short circuit condition on the (001) plane of 2D perovskite bulk crystal (see Figure 3b). Moreover, the relative Raman intensity ratio for the two bands at 1470 and 1484 cm^{-1} on (001) crystal plane changes with the applied bias; while there is no spectral change on the (010) crystal plane under the open and short circuit conditions (Figure S8b, Supporting Information).

According to previous reports,[31,37] the structure of 2D perovskite $(PEA)_2PbBr_4$ can be regarded as a sandwich structure, that is, the $[PbBr_6]^{4-}$ octahedral structure is sandwiched by large-sized layered organic PEA^+ cations which work as insulating barriers and confine the charge carriers within a 2D local regium.[37] The alternating arrangements of inorganic sheets and bulk organic interlayers result in the natural multiple quantum well electronic structure (Figure S11a, Supporting Information). The optimized crystal structures along the *a* and *c* axes are given in Figure S11b, Supporting Information, in which the (001) crystal plane shows periodically layered morphology, in perfect agreement with the 2D layered structure. The obvious changes of the relative band intensity on the (001) crystal plane can be attributed to the spatial confinement of the 2D crystal structure and the dielectric mismatch between the organic and inorganic layers in the (010) plane, leading to strong bound excitons with low mobility.[38] Moreover, due to the weak atomic orbital hybridization of the PEA^+ cations, the charge distribution in the (010) plane is suppressed, resulting in a stronger dispersion of the charge distribution in the valence band maximum and conduction band minimum on the (001) plane than that on the (010) plane, which means that the electron excitation energy on the (001) plane is much lower than that on the (010) plane. Therefore, the carrier transport speed in the (001) plane is significantly higher than that in the (010) plane.[25]

We further perform an internal carrier transport investigation on the 2D perovskite crystal through Raman spectroscopy by tuning the bias from 0 to 30 V (Figure 3c). The variations of the relative Raman intensity at 1470 and 1484 cm^{-1} bands on the
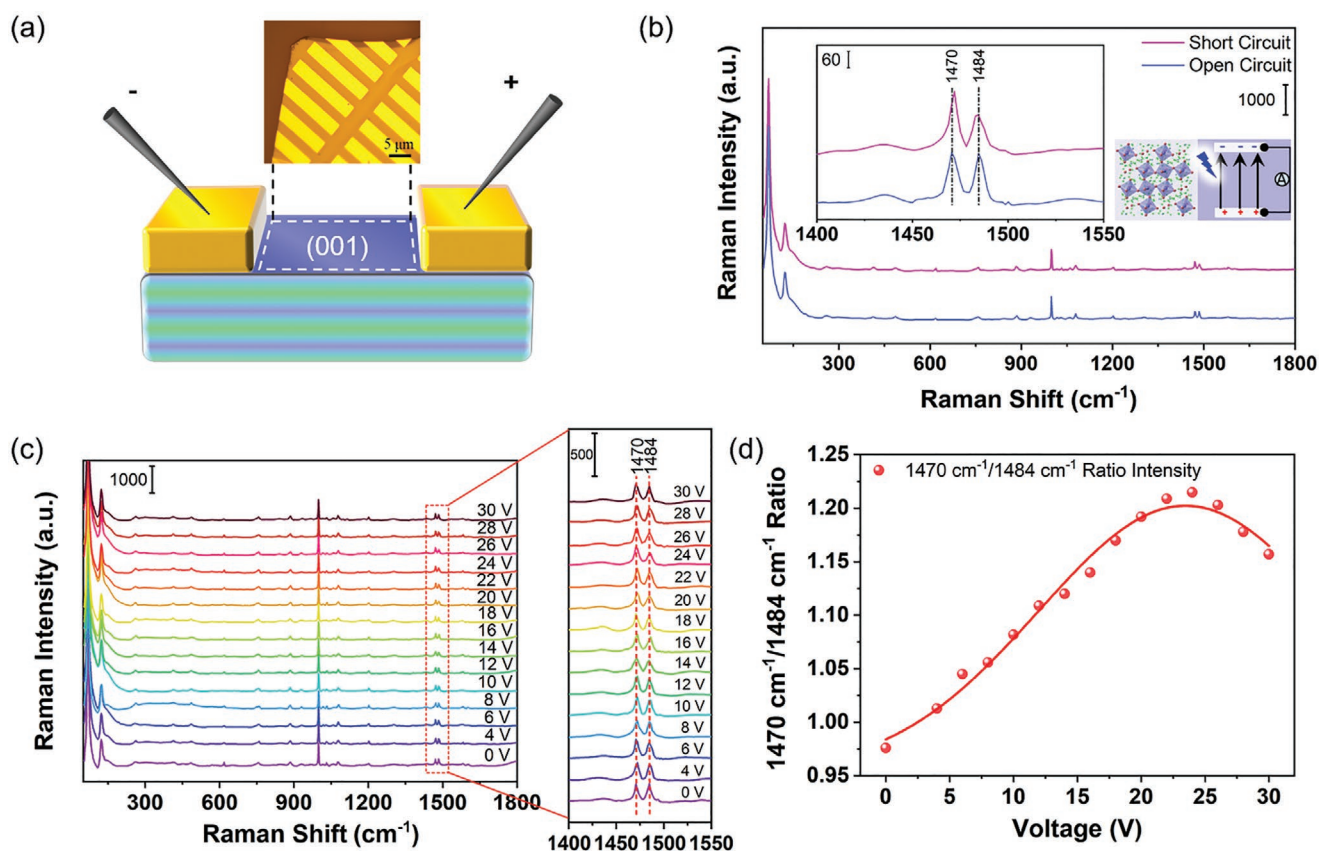
Figure 3. Voltage-dependent intrinsic Raman spectra of bulk 2D perovskite single crystals. a) Schematic of the 2D perovskite crystal devices. b) Raman spectroscopy of the device based on (001) plane of the $(PEA)_2PbBr_4$ single crystal under short circuit and open circuit conditions. c) Raman spectroscopy for the (001) plane device under varying bias voltages. d) The variation in relative Raman intensity of two bands (1470 and 1484 cm^{-1}) as a function of the applied bias voltage in the photodetector made on (001) plane of the bulk 2D perovskite single crystal.

(001) plane are strongly dependent on the applied bias, which shows a trend of the first increasing and then decreasing with the increasing applied bias, with a maximum relative intensity ratio adjustment result at a bias of 24 V (Figure 3d).

2.4. Intrinsic Carrier Transport Mechanism Analysis

To elucidate the underlying carrier transport mechanism behind the varying Raman spectra, theoretical simulation was carried out to explore the process and to explain the above observations. As for the Raman analysis results, the vibration mode of the bands at 1470 and 1484 cm^{-1} can be attributed to the H−C−H bending mode of alkyl chain and C−H in plane bending mode of benzene, respectively (Figure S12, Supporting Information). The −NH$_2$ group of the PEA molecules directly connect to the inorganic layer of the 2D perovskite and a slight electronic perturbation among the inorganic layer will directly affect the polarizability of PEA, resulting in the change of the Raman intensity. To further explore the effect of the electronic perturbation on the vibration mode of organic layers, the molecular orbital and the intramolecular electron transitions of the PEA molecules are further calculated. **Figure 4**a shows the frontier orbitals of the HOMO, LUMO, and LUMO+1 level of the PEA molecules from the DFT simulations. When applied the

bias on the (001) plane, the electrons transit along the inorganic layers and affect the electron density of the PEA molecules. The contribution of the laser-induced electronic transition from the HOMO level to the LUMO+1 level can increase, which further improves the polarizability around the −CH$_2$ group. This phenomenon is proved by the theoretical simulation of electron–hole distribution of the first excited state constructed by the LUMO and LUMO+1 levels with 44% and 56% contributions, respectively, as shown in Figure 4b. The obtained results exhibit an obvious delocalization phenomenon owing to high contribution of LUMO+1; as a result, the relative Raman intensity values of both 1471 and 1484 cm^{-1} can change accordingly.

In the actual situation, the carrier transport properties in halide perovskite single crystals are also severely affected by their inherent charge trap defects, particularly the solution-processed cases. Figure 4c presents the schematic diagram of carrier transport mechanism with the increasing bias. When the appropriate bias is applied, the injected charges will passivate the defects within the perovskite materials,[39,40] and these filled defects will no longer trap the carriers, which would be beneficial for the charge transport and thus lead to the increase in the charges' number in the inorganic layer. Moreover, according to the theoretical simulation, such phenomenon can result in the increased polarizability of PEAs. As a result, the relative Raman spectra intensity increases. However,
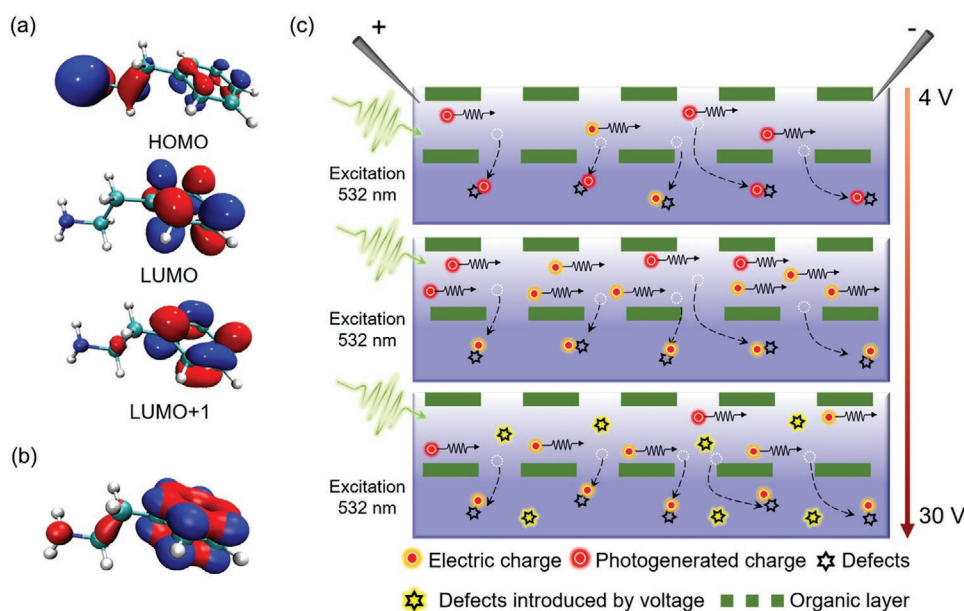
ADVANCED
SCIENCE NEWS
www.advancedsciencenews.com

NANO · MICRO
small
www.small-journal.com

Figure 4. Anisotropic transport mechanism. a) The frontier of the HOMO, LUMO, and LUMO+1 levels of the PEA molecules. b) The electron–hole distribution of the first excited state. The blue and red iso-surfaces represent the hole and electron distributions, respectively. c) The schematic diagram of carrier transport mechanism for 2D perovskite crystal with different bias.

when the excessive bias is applied, the excessive charges will not only passivate the inherent defects of the material but also trap holes through charge recombination. Therefore, the excessive injected charges can act as new additive defects and hinder the transport of carriers, affecting the electronic disturbance in the inorganic layer and further weaken the polarizability of PEA groups.[41,42,43] Meanwhile, the relative Raman intensity decreases accordingly. Besides, for the (010) plane, due to the quantum confinement effect, the extraneous electrons cannot be injected into the perovskite, and the Raman spectra on the (010) plane show nearly no change with the increase of the bias (Figure S8c,d, Supporting Information), which indicates that the carrier transport is blocked by the insulating layers.

According to the above discussions, the polarization on (001) plane leads to the change of charge distribution at the interface of organic and inorganic layers, therefore the vibration mode of the PEA molecules is affected, which shows the changes of the relative intensities at 1471 and 1480 cm^{-1} bands. In the (010) plane case, the electron transition is inhibited, and the electronic environment keeps stable even with the bias applied, while the Raman spectra show no obvious change under this condition. The findings indicate that the (001) plane is more conducive for the carrier transport along the plane of the inorganic sheet in comparison to the (010) plane perpendicular to the sheets, which are affected by the special structure of 2D perovskite. Thus, we can conclude that the electron transition among the perovskites can be intuitively reflected by the Raman spectra of PEA molecules and the Raman spectra measurement can be taken as a powerful route to study the quantum confinement effect accordingly.

To explore the reversibility of the voltage polarization phenomenon, the relative intensities of the bands at 1470 and 1484 cm^{-1} are further investigated on the dependence of the polarization time upon the bias of 6 V on the (001) plane of the bulk (PEA)$_2$PbBr$_4$ single crystal (polarization time of 10 s for each point). As shown in **Figure 5**a, the relative intensity ratio continues to increase, reaching the saturation at 40 s as the polarization time increases; when the voltage is removed, the relative intensity ratio drops rapidly and returns to the initial state before polarization (Figure 5b). The obtained results are further summarized in Figure 5c. Interestingly, the reversible polarization-recovery phenomenon is highly repeatable, indicating high stability of the 2D perovskite crystals. And the relative intensity ratio shows an obvious on/off switching behaviors with the variation of the applied bias in five cycles measurements (Figure 5d and Figures S13–S16, Supporting Information). We also explored the relationship between the Raman spectra of the 2D perovskite on (010) plane and the polarization time (Figure S17, Supporting Information), which shows no significant changes with the increase of polarization time. This should also be attributed to the quantum confinement effect of the 2D perovskite crystals.

3. Conclusion

In conclusion, we investigate the carrier transport properties in 2D perovskite thin crystals through SERS technique. The interfacial and internal charge transfer processes can be clearly monitored by evaluating the vibration mode changes of their Raman spectra. The enhanced Raman spectra of 2D perovskite-based heterojunction with the added PTCDA molecules indicate the interfacial charge transfer process, which can help enhance the photoelectric response properties upon a 532-nm laser irradiation, holding great promise for designing the high-performance optoelectronic devices. Additionally, the thickness-dependent Raman and photocurrent intensities exhibit the consistent change trends for the heterojunctions, that is, first increasing and then decreasing, which can be assigned to the
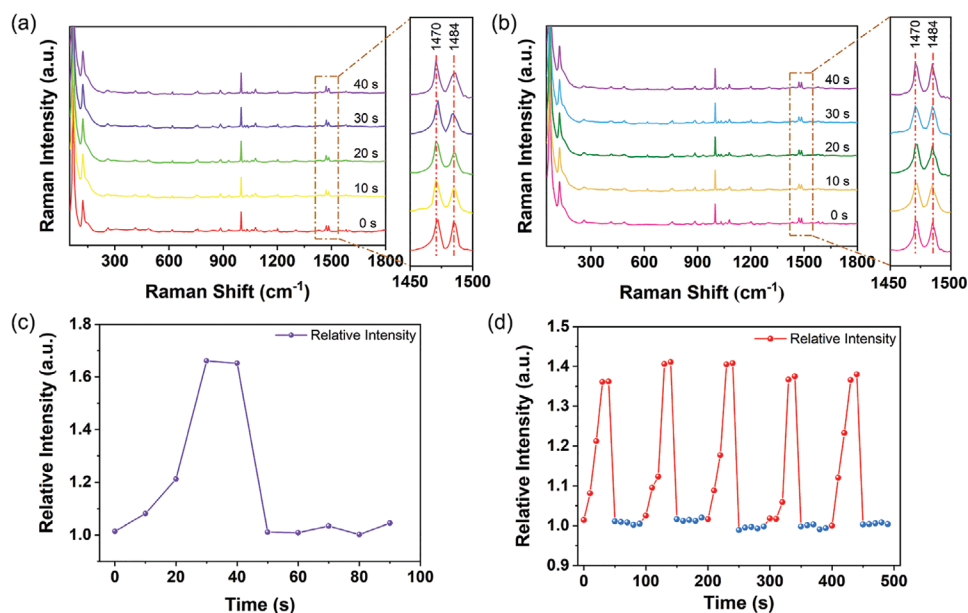
Figure 5. Characterizations of the reversibility of voltage polarization. a) Raman spectra of the device based on (001) plane under different polarizations times with a 6-V bias. b) Raman spectra of device under different delay times after removing voltages. c) The relative intensity ratio of Raman spectra in the two bands (1470 and 1484 cm^{-1}) varies with the applied on/off potential. d) Five cycles of on/off status.

quantum confinement effect within 2D perovskite crystals. Due to the unique structural characteristics, the clear difference of the charge carrier transport modes between in the (001) plane and (010) plane for the bulk 2D perovskite single crystals were obtained. Through the SERS measurements combined with the theoretical simulations, we further investigated systematically the related mechanisms. The anisotropic transport properties along various crystallographic orientation affected by the quantum confinement effect are observed and are identified from the distinct differences in the Raman spectra. This work not only highlights a novel approach for studying carrier transfer model and carrier transport properties within the 2D perovskite crystals but also paves the way for performance enhancement strategies in the related devices in the perspective of Raman spectra, which are thus of significance for optoelectronic device designs and optimizations.

4. Experimental Section

Chemicals: Phenethylammonium bromide (PEABr, ≥99.5%) was purchased from Xi'an Polymer Light Technology Corp. Lead bromide (PbBr$_2$, 99%) was purchased from Aladdin Company. N, N-Dimethylformamide (DMF, 99.8%) was purchased from Sigma-Aldrich. Perylene-3, 4, 9, 10-tetracarboxylic dianhydride (C$_{24}$H$_8$O$_6$, 98%) was purchased from Shanghai Macklin Biochemical Co., Ltd. (China). All the reagents were used as received without further purification.

(PEA)$_2$PbBr$_4$ Single Crystal Synthesis: 1.835 g of PEABr and 2.01 g of PbBr$_2$ were mixed in 4.4 mL DMF and then stirred at room temperature for 24 h to obtain a 0.873 g mL^{-1} perovskite precursor solution. The solution was then filtered using a PTFE filter with a 0.2-μm pore size. 3 mL of the prepared precursor solution was taken and placed in a reaction vessel sealed with a plastic plate. In order to control the evaporation rate of the solution, a few holes with a diameter of 1 mm were on the plastic plate. The reaction vessel was placed at room temperature, and the transparent crystals appear after 24 h.[44,45,46]

Characterization: The optical image was performed by a KEYENCE VK-X200 3D laser scanning microscope. Raman spectra were carried out using a LabRAM HR Evolution Raman spectrometer (Horiba Jobin Yvon). All Raman spectra were collected under the same conditions with an acquisition time of 5 s using a holographic grating of 1200 grooves mm^{-1}. The spectrometer was calibrated with the Raman spectrum of the silicon wafer at 520.7 cm^{-1}. The SEM image and energy dispersive spectrometry mapping result of the (PEA)$_2$PbBr$_4$ single crystal were collected by using a Phenom Pro-X. XRD spectra were measured using a BRUKER D8 FOCUS. The absorption spectra were carried out by an Agilent Cary 5000. The TRPLs were recorded on a home-built confocal microscope (with objective lens N.A. =0.4) using a pulsed supercontinuum laser (OYSL Photonics, SC-Pro, 150 ps pulse lengths) at 2 MHz repetition rate. The focused pump laser power through an objective lens was 0.25 nW. The scattered light from the pump laser to the detector was filtered by a long-pass filter with a 532-nm edge (Semrock). The SPCM-AQRH Single Photo Counting Module (SPCM-AQRH-15, Excelitas Technologies) detected the PL and the lifetime module was TimeHarp 260 P (PicoQuant). AFM characterizations were performed on a Bruker's Dimension Icon system. Photocurrent-voltage characteristics were measured by a Keithley 4200A semiconductor parametric analyzer (Tektronix) with a C-100 probe station from TPSi Company in the air at room temperature. Different biases on the gold electrode were applied through two probes connected with a DC power supply (MCH-K605DN) to measure the Raman spectrum of the 2D perovskite single-crystal bulk.

The Hybrid Photodetector Construction: The prepared (PEA)$_2$PbBr$_4$ thin single crystals were transferred to the SiO$_2$/Si substrate by mechanical peeling, and then the 1-nm PTCDA molecules were vaporized on the thin single crystals through a thermal evaporation-induced assembly method and the 100-nm gold electrodes were vaporized using a mask. The electrode spacing was 20 μm. Finally, the hybrid photodetector can be successfully fabricated.

DFT Calculations: The geometries of PEA were optimized by DFT using the basis set B3LYP with a triple split valence basis set of 6-311+G*. At this geometry, frequency calculation was obtained at the same level, with a scaling factor of 0.9680.[47] The simulated Raman spectra were performed with Lorentzian expansion in a line width of 10 cm^{-1} at laser line 532 nm and 298 K. And electronic transitions were calculated with time-dependent DFT, which only singlet-singlet excitations were

evaluated. The wavefunction analysis and visualization of energy levels of molecules were performed by Multiwfn and VMD.[48,49] All calculations were carried out by the Gaussian 09 program.[50]

Supporting Information

Supporting Information is available from the Wiley Online Library or from the author.

Acknowledgements

Conflict of Interest

The authors declare no conflict of interest.

Data Availability Statement

The data that support the findings of this study are available from the corresponding author upon reasonable request.

Keywords

[1] G. H. Xing, N. Mathews, S. Y. Sun, S. S. Lim, Y. M. Lam, M. Gratzel, S. Mhaisalkar, T. C. Sum, *Science* **2013**, *342*, 344.
[2] S. D. Stranks, G. E. Eperon, G. Grancini, C. Menelaou, M. J. P. Alcocer, T. Leijtens, L. M. Herz, A. Petrozza, H. J. Snaith, *Science* **2013**, *342*, 341.
[3] C. Wehrenfennig, G. E. Eperon, M. B. Johnston, H. J. Snaith, L. M. Herz, *Adv. Mater.* **2014**, *26*, 1584.
[4] S. D. Stranks, H. J. Snaith, *Nat. Nanotechnol.* **2015**, *10*, 391.
[5] O. Malinkiewicz, A. Yella, Y. H. Lee, G. M. Espallargas, M. Graetzel, M. K. Nazeeruddin, H. J. Bolink, *Nat. Photonics* **2013**, *8*, 128.
[6] H. Wang, D. H. Kim, *Chem. Soc. Rev.* **2017**, *46*, 5204.
[7] X. Hu, X. Zhang, L. Liang, J. Bao, S. Li, W. Yang, Y. Xie, *Adv. Funct. Mater.* **2014**, *24*, 7373.
[8] J. S. Huang, Y. B. Yuan, Y. C. Shao, Y. F. Yan, *Nat. Rev. Mater.* **2017**, *2*, 17042.
[9] D. Shi, V. Adinolfi, R. Comin, M. J. Yuan, E. Alarousu, A. Buin, Y. Chen, S. Hoogland, A. Rothenberger, K. Katsiev, Y. Losovyj, X. Zhang, P. A. Dowben, O. F. Mohammed, E. H. Sargent, O. M. Bakr, *Science* **2015**, *347*, 519.
[10] Q. F. Dong, Y. J. Fang, Y. C. Shao, P. Mulligan, J. Qiu, L. Cao, J. S. Huang, *Science* **2015**, *347*, 967.
[11] A. Younis, C. H. Lin, X. W. Guan, S. Shahrokhi, C. Y. Huang, Y. T. Wang, T. Y. He, S. Singh, L. Hu, J. R. D. Retamal, J. H. He, T. Wu, *Adv. Mater.* **2021**, *33*, 2005000.
[12] Z. Wang, Z. J. Shi, T. T. Li, Y. H. Chen, W. Huang, *Angew. Chem., Int. Ed.* **2017**, *56*, 1190.
[13] Q. Wang, B. Chen, Y. Liu, Y. H. Deng, Y. Bai, Q. F. Dong, J. S. Huang, *Energy Environ. Sci.* **2017**, *10*, 516.
[14] X. Zhang, R. Munir, Z. Xu, Y. C. Liu, H. Tsai, W. Y. Nie, J. B. Li, T. Q. Niu, D. M. Smilgies, M. G. Kanatzidis, A. D. Mohite, K. Zhao, A. Amassian, S. Z. Liu, *Adv. Mater.* **2018**, *30*, 1707166.
[15] P. R. Cheng, Z. Xu, J. B. Li, Y. C. Liu, Y. Y. Fan, L. Y. Yu, D. M. Smilgies, C. Muller, K. Zhao, S. Z. Liu, *ACS Energy Lett.* **2018**, *3*, 1975.
[16] M. Shimizu, J. Fujisawa, T. Ishihara, *Phys. Rev. B* **2006**, *74*, 155206.
[17] Z. Fang, X. M. Hou, Y. P. Zheng, Z. B. Yang, K. C. Chou, G. Shao, M. H. Shang, W. Y. Yang, T. Wu, *Adv. Funct. Mater.* **2021**, *31*, 2102330.
[18] L. Etgar, *Energy Environ. Sci.* **2018**, *11*, 234.
[19] B. Saparov, D. B. Mitzi, *Chem. Rev.* **2016**, *116*, 4558.
[20] S. Yang, Y. Wang, P. Liu, Y. B. Cheng, H. J. Zhao, H. G. Yang, *Nat. Energy* **2016**, *1*, 15016.
[21] K. B. Zheng, T. Pullerits, *J. Phys. Chem. Lett.* **2019**, *10*, 5881.
[22] N. N. Wang, L. Cheng, R. Ge, S. T. Zhang, Y. F. Miao, W. Zou, C. Yi, Y. Sun, Y. Cao, R. Yang, Y. Q. Wei, Q. Guo, Y. Ke, M. T. Yu, Y. Z. Jin, Y. Liu, Q. Q. Ding, D. W. Di, L. Yang, G. C. Xing, H. Tian, C. H. Jin, F. Gao, R. H. Friend, J. P. Wang, W. Huang, *Nat. Photonics* **2016**, *10*, 699.
[23] C. M. M. Seo, W. Y. Nie, C. C. Stoumpos, H. Tsai, J.-C. Blancon, F. Z. Liu, J. Even, T. J. Marks, A. D. Mohite, M. G. Kanatzidis, *Adv. Energy Mater.* **2018**, *8*, 1700979.
[24] A. Z. Chen, M. Shiu, X. Y. Deng, M. Mahmoud, D. P. Zhang, B. J. Foley, S. H. Lee, G. Giri, J. J. Choi, *Chem. Mater.* **2019**, *31*, 1336.
[25] Y. C. Liu, H. C. Ye, Y. X. Zhang, K. Zhao, Z. Yang, Y. B. Yuan, H. D. Wu, G. T. Zhao, Z. P. Yang, J. Tang, Z. Xu, S. Z. Liu, *Matter* **2019**, *1*, 465.
[26] M. Fleischmann, P. J. Hendra, A. J. Mcquillan, *Chem. Phys. Lett.* **1974**, *26*, 163.
[27] J. R. Lombardi, R. L. Birke, *J. Phys. Chem. C* **2008**, *112*, 5605.
[28] S. E. J. Bell, N. M. S. Sirimuthu, *Chem. Soc. Rev.* **2008**, *37*, 1012.
[29] S. Park, P. X. Yang, P. Corredor, M. J. Weaver, *J. Am. Chem. Soc.* **2002**, *124*, 2428.
[30] W. Ji, Y. Kitahama, X. X. Xue, B. Zhao, Y. Ozaki, *J. Phys. Chem. C* **2012**, *116*, 2515.
[31] Z. H. Sun, C. X. Wang, J. X. Yang, B. Zhao, J. R. Lombardi, *J. Phys. Chem. C* **2008**, *112*, 6093.
[32] P. Tarakeshwar, J. L. Palma, D. Finkelstein-Shapiro, A. Keller, I. Urdaneta, M. Calatayud, O. Atabek, V. Mujica, *J. Phys. Chem. C* **2014**, *118*, 3774.
[33] Y. X. Zhang, Y. C. Liu, Z. Xu, H. C. Ye, Q. X. Li, M. X. Hu, Z. Yang, S. Z. Liu, *J. Mater. Chem. C* **2019**, *7*, 1584.
[34] P. Alessio, M. L. Braunger, R. F. Aroca, C. A. Olivati, C. J. L. Constantino, *J. Phys. Chem. C* **2015**, *119*, 12055.
[35] X. X. Han, W. Ji, B. Zhao, Y. Ozaki, *Nanoscale* **2017**, *9*, 4847.
[36] J. Xing, Y. T. Zou, C. Zhao, Z. Yu, Y. W. Shan, W. C. Kong, X. Zheng, X. Y. Li, W. L. Yu, C. L. Guo, *Mater. Today Phys.* **2020**, *14*, 100240.
[37] D. B. Mitzi, *J. Mater. Chem.* **2004**, *14*, 2355.
[38] E. A. Muljarov, S. G. Tikhodeev, N. A. Gippius, T. Ishihara, *Phys. Rev. B* **1995**, *51*, 14370.
[39] I. A. Shkrob, T. W. Marin, *J. Phys. Chem. Lett.* **2014**, *5*, 1066.
[40] H. H. Fang, S. Adjokatse, H. T. Wei, J. Yang, G. R. Blake, J. S. Huang, J. Even, M. A. Loi, *Sci. Adv.* **2016**, *2*, e1600534.
[41] J. Xing, C. Zhao, Y. T. Zou, W. C. Kong, Z. Yu, Y. W. Shan, Q. F. Dong, D. Zhou, W. L. Yu, C. L. Guo, *Light: Sci. Appl.* **2020**, *9*, 111.
[42] B. Chen, P. N. Rudd, S. Yang, Y. B. Yuan, J. S. Huang, *Chem. Soc. Rev.* **2019**, *48*, 3842.
[43] M. H. Kang, S. H. Kim, S. Jang, J. E. Lim, H. Chang, K.-j. Kong, S. Myung, J. K. Park, *RSC Adv.* **2018**, *8*, 28447.

[44] D. Liang, Y. L. Peng, Y. P. Fu, M. J. Shearer, J. J. Zhang, J. Y. Zhai, Y. Zhang, R. J. Hamers, T. L. Andrew, S. Jin, *ACS Nano* **2016**, *10*, 6897.

[45] D. W. Ma, Y. P. Fu, L. N. Dang, J. Y. Zhai, I. A. Guzei, S. Jin, *Nano Res.* **2017**, *10*, 2117.

[46] C. Y. Ge, W. H. Zhai, C. Tian, S. Q. Zhao, T. Guo, S. R. Sun, W. X. Chen, G. Z. Ran, *RSC Adv.* **2019**, *9*, 16779.

[47] J. P. Merrick, D. Moran, L. Radom, *J. Phys. Chem. A* **2007**, *111*, 11683.

[48] T. Lu, F. W. Chen, *J. Comput. Chem.* **2012**, *33*, 580.

[49] W. Humphrey, A. Dalke, K. K. Schulten, *J. Mol. Graphics* **1995**, *14*, 33.

[50] M. J. Frisch, G. W. Trucks, H. B. Schlegel, G. E. Scuseria, M. A. Robb, J. R. Cheeseman, G. Scalmani, V. Barone, B. Mennucci, G. A. Petersson, H. Nakatsuji, M. Caricato, X. Li, H. P. Hratchian, A. F. Izmaylov, J. Bloino, G. Zheng, J. L. Sonnenberg, M. Hada, M. Ehara, K. Toyota, R. Fukuda, J. Hasegawa, M. Ishida, T. Nakajima, Y. Honda, O. Kitao, H. Nakai, T. Vreven, J. A. Montgomery Jr., J. E. Peralta, F. Ogliaro, M. Bearpark, J. J. Heyd, E. Brothers, K. N. Kudin, V. N. Staroverov, T. Keith, R. Kobayashi, J. Normand, K. Raghavachari, A. Rendell, J. C. Burant, S. S. Iyengar, J. Tomasi, M. Cossi, N. Rega, J. M. Millam, M. Klene, J. E. Knox, J. B. Cross, V. Bakken, C. Adamo, J. Jaramillo, R. Gomperts, R. E. Stratmann, O. Yazyev, A. J. Austin, R. Cammi, C. Pomelli, J. W. Ochterski, R. L. Martin, K. Morokuma, V. G. Zakrzewski, G. A. Voth, P. Salvador, J. J. Dannenberg, S. Dapprich, A. D. Daniels, O. Farkas, J. B. Foresman, J. V. Ortiz, J. Cioslowski, D. J. Fox, *Gaussian 09, Revision D.01*, Gaussian, Inc, Wallingford CT, **2013**.